ACS Photonics

pubs.acs.org/journal/apchd5

Letter

Harmonic Resonance Enhanced Second-Harmonic Generation in the Monolayer WS_2–Ag Nanocavity

Xiaobo Han, Kai Wang,* Patrick D. Persaud, Xiangyuan Xing, Weiwei Liu, Hua Long, Fang Li, Bing Wang, Mahi R. Singh,* and Peixiang Lu*

Cite This: *ACS Photonics* 2020, 7, 562–568

Read Online

ACCESS | Metrics & More | Article Recommendations | Supporting Information

ABSTRACT: The enhanced second-harmonic generation (SHG) from a monolayer WS_2 coupled to a plasmonic nanocavity is experimentally and theoretically investigated. The nanocavity is comprised of monodispersed Ag nanocubes separated from an Ag film by a spacer Al_2O_3, namely, the nanoparticle on mirror (NPoM) system. When the surface plasmon polariton resonance (SPPR) wavelength of NPoM nanocavity overlaps well with the SHG wavelength of the monolayer WS_2 (namely, harmonic resonance), a ~300-fold SHG enhancement is achieved in experiment. For theoretical understanding, the quantum mechanical density matrix method has been used to develop a theory for SHG. It is found that the SHG intensity of nanohybrid is proportional to the square of the local-field intensity in NPoM nanocavity at SHG wavelength, which is ascribed to the dipole–quadrupole interaction between dipole, P_{SHG}, in the monolayer WS_2 and quadrupole, Q_{Ag}, in Ag nanocavity. It is significantly different from that in metal nanoparticles under harmonic resonance, which is proportional to the local-field intensity. Therefore, it provides a novel mechanism for enhancing SHG signals from metal–semiconductor nanohybrids, which has potential applications in nonlinear devices and hybrid nonlinear metasurfaces.

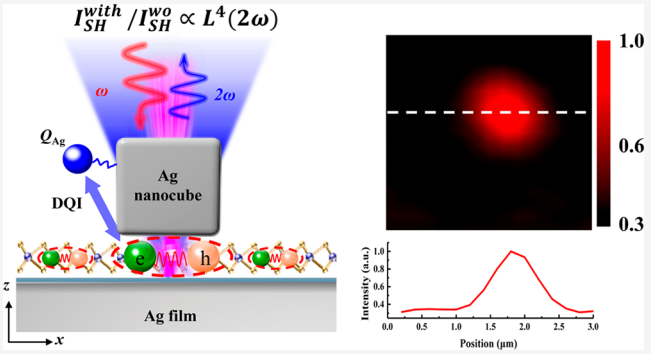

KEYWORDS: *second-harmonic generation, plasmonic nanocavity, monolayer WS_2, Ag nanocube, dipole–quadrupole interaction*

Second-harmonic generation (SHG) is an important second-order nonlinear optical response, which converts two photons of frequency ω into another photon of double frequency 2ω.[1] Recently, SHG in semiconductor nanostructures, such as ZnS, GaAs nanowire, and monolayers MoS_2,[2−5] has attracted much attention due to its potential applications in coherent nanosources,[5,6] imaging,[7−9] and nanoprobing.[2,10−13] However, the SHG process is generally weak at the subwavelength scale, since second-order nonlinear effects scale quadratically with the volume of the nanostructure.[14] Therefore, it is still faced with challenges to boost nonlinear conversion efficiency. Many works have focused on the enhanced nonlinear optical properties in the noble metal–semiconductor nanohybrids with a well designing.[14−23] Owing to a unique optical property called surface plasmon polaritons resonance (SPPR) in noble metals, the intensity of local-field can be efficiently concentrated which is ideal for enhancing nonlinear processes, such as SHG,[18−22] third-harmonic generation (THG),[24] and two-photon luminescence (TPL).[25,26]

In general, the SPPR wavelength in metal–semiconductor nanohybrids is usually designed to be resonant with the pumping wavelength, which is known as fundamental resonance. Since the fundamental local-field is boosted, the generated SHG signals can be efficiently enhanced by square of the fundamental local-field intensity.[20,21] However, the fundamental resonance can strongly enhance the absorption of the pumping laser, which may easily cause heat damage or unwanted signals, such as supercontinuum.[27] Therefore, a limited intensity of the pumping laser can be allowed. For improving SHG conversion efficiency, the SPPR wavelength is also tuned to match with the SHG wavelength shown in Figure 1a, which is called a harmonic resonance.[28] Since SHG intensity is in proportion to the local-field intensity at SHG wavelength, the SHG signal generally can only be enhanced by 1 order of magnitude.[29,30] As reported, a few works study the harmonic resonance enhanced SHG in pure metal nanoparticles (NPs).[30−32] To our knowledge, the harmonic resonance enhanced SHG in metal–semiconductor nanohybrids is still not addressed clearly.

On the other hand, two-dimensional transition-metal dichalcogenides (TMDs) have drawn a lot of interest in

Received: October 14, 2019
Published: February 4, 2020

https://dx.doi.org/10.1021/acsphotonics.9b01499
ACS Photonics 2020, 7, 562–568

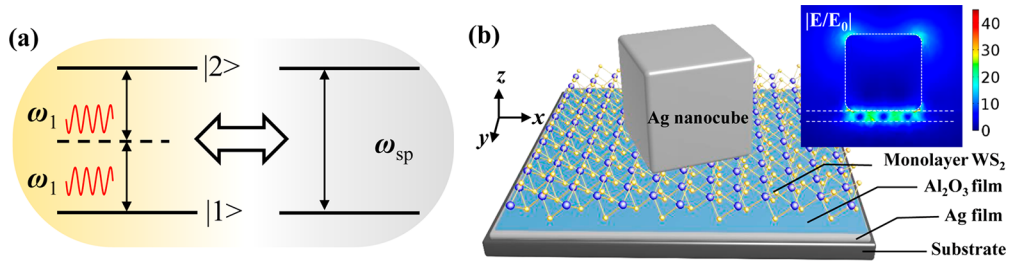

Figure 1. (a) An energy level schematic diagram of the hybrid metal−semiconductor system. The semiconductor material is made of two levels denoted as |1> and |2>, where |1> is the ground state. ω_1 and ω_{sp} denote the pumping laser frequency and SPPR frequency of metal NPs, respectively. When $2\omega_1 = \omega_{sp}$, there is a strong interaction between semiconductor materials and metal NPs. (b) A schematic diagram of the designed hybrid system. Plasmonic nanocavity is composed of single Ag nanocubes and an Ag film. A monolayer WS_2 is placed in the nanocavity. The inset shows the calculated electric field of $|E/E_0|$ in the *xz*-plane at resonances wavelength. White lines indicate the outline of the Ag nanocube with length of ∼75 nm.

recent years due to the unique optical[3,11,33] and electrical properties.[34] Since the thickness of monolayer TMDs is less than 1 nm, many previously used nanohybrids are not applicable, such as core−shell and strip-covered structures.[14,21,22] Therefore, a highly confined nanocavity, namely, nanoparticle on mirror (NPoM), is introduced for monolayer TMDs. It is composed of monodispersed metal NPs separated from a metal film by a spacer, and a monolayer TMD is placed in the nanogap.[35,36] It has many advantages that cavity mode and resonance peaks can be easily tuned by NP size, shape, and the thickness of spacer layers.[37−40] It has been reported that the strong coupling[41,42] and the large PL enhancement in monolayer TMDs are observed with the nanocavity.[43]

In this work, Ag NPoM nanocavity are designed and coupled with monolayer WS_2 to enhance the SHG signals. The nanocavity consists of Ag nanocubes over an Ag film, separated by an Al_2O_3 layer (<10 nm). By detuning the SPPR wavelength of nanocavity to the SHG wavelength at 410 nm, a large SHG enhancement factor (EF) of ∼300 is achieved experimentally. For understanding the enhancement mechanism, a theoretical model of semiconductor and nanocavity interaction is used. It demonstrates that the SHG intensity is proportional to the square of the local-field intensity of the Ag nanocavity at the SHG wavelength, which is caused by the dipole−quadrupole interaction between dipole, P_{SHG}, in the monolayer WS_2 and quadrupole, Q_{Ag}, in the Ag nanocavity. It shows a significant difference with that in pure metal NPs under harmonic resonance, which is in proportion to the local-field intensity. Therefore, it reveals a clearly underlying mechanism for the SHG enhancement by harmonic resonance and provides further exploration for nonlinear enhancement of metal−semiconductor hybrid structures.

Figure 1b shows the schematic diagram of the monolayer WS_2−Ag NPoM nanocavity. It is composed of an Ag film, an Al_2O_3 film, and a single Ag nanocube, where a monolayer WS_2 is placed on the Al_2O_3 film. Broadband tuning of the Ag nanocube plasmon resonance can be achieved due to strong electromagnetic coupling between the metal NPs and the film. An alternative approach to realize tuning the SPPR is to change the thickness of Al_2O_3 spacer film. Since the thickness of the Al_2O_3 film is usually quite small (<10 nm), it leads to a strong local field in the NPoM nanocavity. The inset of Figure 1b shows the calculated local-field distribution in the NPoM nanocavity by COMSOL Multiphysics software. The plasmonic nanocavity was fabricated using a bottom-up method. First, a Ti/Ag thin film of thickness ∼10/80 nm was prepared on a silicon substrate via electron beam evaporation. Next, ∼9 nm Al_2O_3 spacer film was deposited by atomic layer deposition (ALD) at the temperature of 100 °C. WS_2 flakes (SixCarbon Tech. Shenzhen) were grown on sapphires by chemical vapor deposition (CVD) method. Avoiding introducing dusts, we transferred WS_2 flakes from the sapphire to the Al_2O_3−Ag film with the help of polydimethylsiloxane (PDMS).[44] Finally, 10 μL of diluted Ag nanocubes (nanoComposix, 0.01 mg/mL) were directly dropped on the prepared substrate. After 1 min, the nanocubes solution was washed off with water, and the sample was dried with nitrogen gas. Ag nanocubes were monodispersed on the Al_2O_3−Ag film uniformly.

Figure 2a shows the schematic experimental setup for individual Ag nanocubes optical measurement. Figure 2b shows an optical microscope image of the nanohybrid: the yellow region is the area of the monolayer WS_2, while the small spots indicate individual Ag nanocubes. The inset in Figure 2b is the transmission electron microscopy (TEM, Tecnai G20) image of a single Ag nanocube with a length of ∼75 nm. Atomic force microscopy (AFM) measurement shows that the thickness of WS_2 is ∼0.7 nm, indicating a monolayer WS_2 is

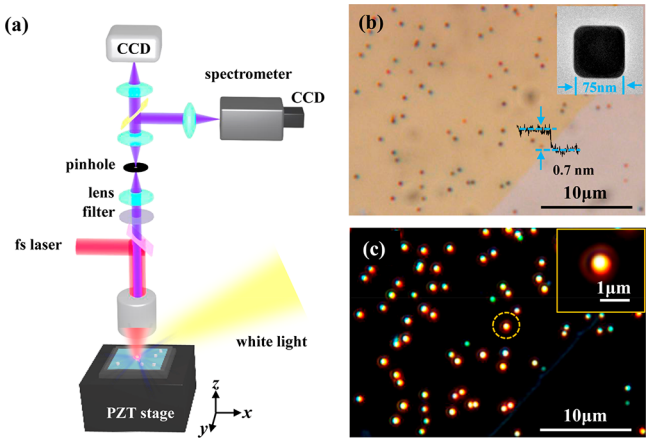

Figure 2. (a) Experimental setup for measuring dark-field scattering signals of individual NPs and SHG signals of the nanohybrids. An oblique incident white light was used for the scattering measurement. (b) Optical image of the nanohybrid, the yellow flakes represent the monolayer WS_2, and small dark spots represent individual Ag nanocubes. TEM image of an Ag nanocube and the thickness of a monolayer WS_2 is shown in the insets. (c) Dark-field scattering image corresponding to (b). Bright spots represent individual Ag nanocubes corresponding to the dark spots in (b). The inset shows the NP image marked with a circle selected by a pinhole.

https://dx.doi.org/10.1021/acsphotonics.9b01499
ACS Photonics 2020, 7, 562−568

used in experiment. Raman spectrum of WS_2 is shown in Figure S1, which is also confirmed for the monolayer nature. For dark-field scattering measurements, an oblique (about 45°) white light (Energetiq, EQ-99XFC) was focused by a lens of 5 cm and illuminated the sample. Scattering light was collected by an objective (Olympus, 50×, NA = 0.5, LMPLanFL N) and focused by a lens again. The focus plane falls on the image plane, where a pinhole (200 μm) was placed to choose individual NPs, as shown in the inset of Figure 2c. Then the scattering light through two lenses was sent to a CCD (Qimaging, QICAM B series) or a spectrometer (Princeton Instruments Acton 2500i with Pixis CCD camera). Figure 2c shows the dark-field scattering image of the same sample corresponding to Figure 2b. The size of Ag nanocubes is distributed from 65 to 95 nm (see Figure S2); therefore, different colors can be observed due to the varied scattering SPPR wavelength of Ag nanocubes with different sizes. The blue line in Figure 2c indicates the edge of the monolayer WS_2. In order to avoid coupling among Ag nanocubes, a proper distribution of nanocubes is necessary.

Figure 3a shows the measured scattering spectra of single Ag nanocubes. It is worth noting that the single nanocavity has

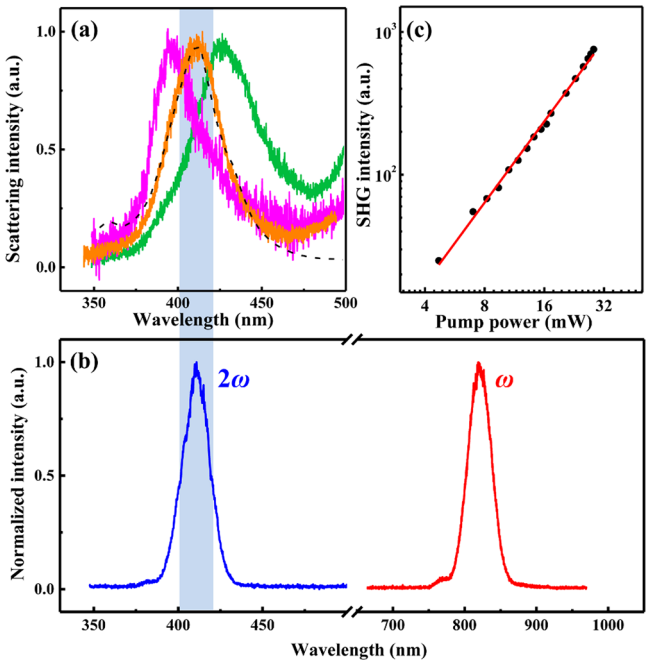

Figure 3. (a) Normalized dark-field scattering intensity of single nanocubes with difference lengths (65∼95 nm). A simulated scattering result is shown as a black dash-dot curve. (b) Measured laser spectrum (red) and its corresponding measured SHG spectrum (blue). (c) SHG intensity response as a function of the excitation (average) power on a log−log scale, which fits to a linear line with a slope about 2.

two SPPR wavelengths shown in Figure S3, so the scattering spots of Ag nanocubes in Figure 2c are not shown in blue colors. Due to size distribution of Ag nanocubes, the measured SPPR peaks are varied from ∼400 to ∼430 nm in Figure 3a. A black dash line indicates the simulated scattering spectrum, which is calculated by COMSOL Multiphysics software under a linear plane wave with a normal incidence. It is in good agreement with the experimental result (detailed parameters of the simulation are presented in the Supporting Information).

According to the definition of the quality factor,[45] $Q = \omega_r/\Delta\omega$, where ω_r and $\Delta\omega$ are the resonance frequency and full-width at half-maximum (fwhm), respectively, the Q factor is ∼8 calculated from Figure 3a. Though it shows a a relatively low Q factor of nanocavity, the nanoscale mode volume still results in a strong local-field.

The nonlinear optical properties of the monolayer WS_2 were measured by a home-built microscopy system, as schematically illustrated in Figure 2a. To measure the SHG signal of the monolayer WS_2, a mode-locked Ti-sapphire femtosecond laser system (Vitara Coherent, ∼ 820 nm, 20 fs and 80 MHz) was focused by a 100× objective (Olympus, NA = 0.8, LMPlanFl) to a spot diameter of ∼1 μm. The radiated signals were collected by the same objective. A 720 nm short pass filter (Semrock, FF01−720/SP-25) was used to avoid the pumping laser. Another 400 nm band-pass filter was used before spectrometer to avoid TPL signals, when doing scanning tests. Same as the scattering optical path, the radiated signals through three lenses were sent to a CCD camera or a spectrometer. In Figure 3b, it indicates the measured optical signal (blue curve) is located at ∼410 nm in the monolayer WS_2 on the Al_2O_3−Ag film, which is exactly twice the frequency of the pumping laser (red curve) at 820 nm. Furthermore, the signal intensity as a function of the pumping power is plotted in Figure 3c. The linear fit with a slope of about 2 indicates the quadratic dependence between the signal intensity and the pumping power. Thus, it is confirmed that the measured signal is attributed to SHG characteristics. Through a reflective neutral density filter (Thorlabs, NDC-50C-4M), the laser intensity in experiment is controlled below 10 kW cm^{-2} to avoid photo damage of nanohybrids. Figure S4 shows the scattering spectra of nanohybrids before and after SHG measurement. Note that no SHG responses from Ag nanocubes or Ag films can be obtained under a relatively low pumping in experiment.

In order to investigate the SHG EF, the SHG scanning measurement is performed. A PZT stage (XMT, XE501-D) was used to move samples in *xy*-plane with a step of 200 nm. Since the average local-field intensity near Ag nanocubes is independent of the laser polarization (see Supporting Information for details), a linearly polarized pumping laser is used. Figure 4a shows the SHG intensity map (3×3 μm^2) of the nanohybrid. It can be observed that the SHG intensity with the Ag nanocube is much stronger than that without nanocube (monolayer WS_2 on the Al_2O_3−Ag film). For a specific

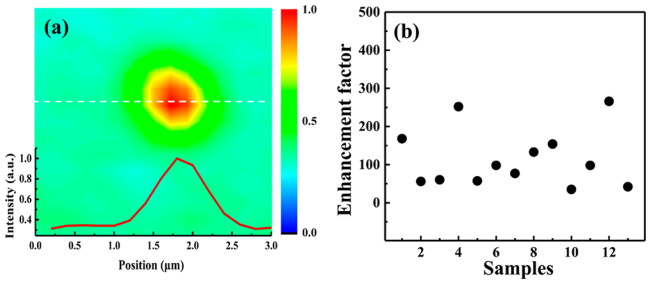

Figure 4. (a) Normalized SHG intensity map of a monolayer WS_2 inserted in a plasmonic nanocavity with a scanning step of 200 nm. The displayed scanning area is 3 μm × 3 μm. The inset curve shows extracted-line (white dash line) intensity marked in the map. (b) SHG EF with different Ag nanocubes under the fixed excitation laser with wavelength of 820 nm.

https://dx.doi.org/10.1021/acsphotonics.9b01499
ACS Photonics 2020, 7, 562−568

comparison, SHG intensity profile across the center of the Ag nanocube is shown in Figure 4a (white dashed line). By comparing the SHG intensity with and without the Ag nanocube, it indicates a 3-fold SHG enhancement. Considering the fact that the size of the Ag nanocube is much smaller than the diameter of the pumping focal spot (~1 μm), the averaged SHG EF across a single nanocavity is defined as

$$\mathrm{EF} = \left(\frac{I_{\mathrm{cavity}}}{I_0} - 1\right)\frac{S_0}{S_{\mathrm{cavity}}} \tag{1}$$

where I_{cavity} is the SHG intensity from the monolayer WS_2 placed in Ag nanocavity and I_0 is the SHG intensity from WS_2 on an Al_2O_3−Ag film. S_0 is the area of the focused spot of the pumping laser, S_{cavity} (~75 × 75 nm^2) is the area of the nanocavity. Finally, the average SHG EF is estimated to be 280 in Figure 4a. Since EF should be very sensitive to the spectral overlap, SHG intensity maps in several samples with different Ag nanocubes are measured shown in Figure 4b. The estimated EF is from 42 to 280. This variation of the EF is mainly ascribed to the spectrally shift of SPPR in the nanocavity due to a slight size variation of the Ag nanocubes. The correlation of EF and SPPR under a fixed excitation (shown in Figure S5) also confirms the sensitivity.

Moreover, SHG EF as a function of the fundamental wavelength (λ_{exc}) from 790 to 840 nm is measured in the same nanocavity. As shown in Figure 5a (red dots), the maximum

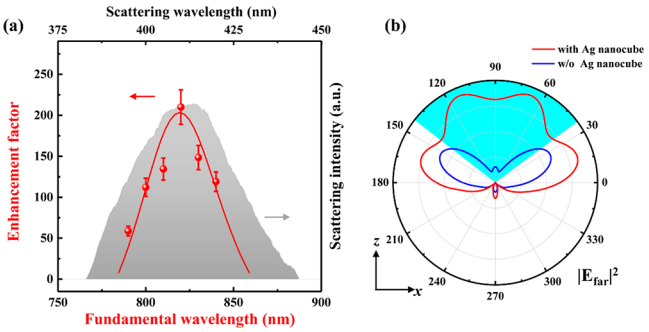

Figure 5. (a) Plot of the SHG EF as a function of excitation laser wavelength in the same nanocavity. The red dots and curve represent the experimental data and theoretical calculations, respectively. The normalized linear scattering spectrum of the nanocavity is shown as a gray area. (b) Radiation pattern of the simulated far-field intensity plotted in the *xz*-plane. The dipole with a wavelength of 410 nm is used to calculate. The blue area shows the collection cone of the objective.

EF of 220 is obtained at wavelength of 820 nm. Gray area in Figure 5a presents the linear scattering spectrum of the nanocavity with the center wavelength at 410 nm. We found that the largest EF is obtained when the SHG wavelength is matched with the peak of the quadrupole mode of the nanocavity at 410 nm, which is half of the excitation wavelength of 820 nm. When the excitation wavelength moves to 790 nm, EF decreases to ~50. It indicates that the EF is very sensitive to the spectra overlap between linear scattering and SHG spectrum. More similar results are shown in Figure S6.

In order to analyze reasons for the SHG enhancement, the radiation pattern of SHG is simulated, since the angular emission pattern of SHG signals can be modified by the Ag nanocube. The SHG radiation is simulated by placing a dipole between Ag nanocube and the Al_2O_3−Ag film (see Supporting Information for simulated details). As shown in Figure 5b, red and blue curves present the emission pattern in the *xz*-plane with and without Ag nanocube, respectively. Since the collection angular (pale blue area) is determined by an objective with NA = 0.8, up to ~5-fold enhancement in SHG collection efficiency is obtained. Note that the charge transfer process between monolayer WS_2 and Ag nanocubes is prohibited in our experiment, due to the PVP coated the Ag nanocubes. Therefore, the hot carrier injection did not happen which is also useful for SHG enhancement.[46] Additionally, the polarization of the emitted SH signal should also be considered. Because the WS_2/Ag nanostructure shows a quadrupole SH emission while the pure monolayer WS_2 is a dipole type, which might be influenced by the out-coupling efficiency. We have checked the experiment setup, especially the reflective mirror used for SH emissions. The reflectance of Ag mirror (Thorlabs, PFR10-P01) shows a small variation of 0.3% between p- and s-polarization light at 410 nm. It indicates that the out-coupling efficiency have little influence on the estimated EF.

For further understanding the SHG enhancement mechanism, we develop a theoretical model for the SHG enhancement of nanohybrids based on the theory developed by Singh.[47] The nanohybrid is made of a plasmonic nanocavity doped with quantum emitters (QEs), which is similar to the experimental samples. The monolayer WS_2 acts as the QE. A strong probe field with frequency ω_1 is applied to create two-photon absorption in the nanohybrid. The SHG signals are produced by QEs. We consider that the QE is made of two energy levels denoted as |1> and |2>, where |1> is the ground state. The frequency difference between states |1> and |2> is denoted as ω_{12}. A schematic diagram of the QE is shown in Figure 1a. Surface plasmon polaritons (SPPs) and SPPRs are present at the interfaces of the Ag nanocube and the Ag film. The probe field acts between the transitions |1> ↔ |2>, giving us the condition of $\omega_{12} = 2\omega_1$. The SPP field of the nanocube and the SPP field produced by the Ag film also act between the transitions |1> ↔ |2>. The SHG emission occurs between the transition of |1> ↔ |2> due to two photons ($2\omega_1$), giving us the condition $\omega_{12} = 2\omega_1$.

We calculate SPP electric field emitted by the Ag nanocube. We denote the dielectric constant of the Ag nanocube as ϵ_c, and the dielectric constant for the WS_2 layer (the QE) as ϵ_q. We apply a probe field with an amplitude E_p, frequency ω_1, and wavelength λ. When the probe field falls on an Ag nanocube, induced dipole and quadrupole moments are produced in the Ag nanocube. Due to the dipole mode is not resonance with the ω_{12} or $2\omega_1$, here only the quadrupole mode is calculated. Dipole mode of Ag nanocubes and SPP field produced by the Ag film are calculated in the Supporting Information. The induced quadrupole moment produces the SPP quadrupole electric field. The field can be calculated using the quasi-static approximation.[48−52] Let $E_{\mathrm{QP}}^{\mathrm{cube}}$ be the electric fields produced by the quadrupole moment. By solving the Maxwell equations in the static wave approximation, the electric field produced by the Ag nanocube is calculated as

$$E_{\mathrm{QP}}^{\mathrm{cube}} = (\Pi_{\mathrm{QP}}^{\mathrm{cube}})E_p, \quad \Pi_{\mathrm{QP}}^{\mathrm{cube}} = \frac{V_{\mathrm{cube}}^{5/3}\zeta_{\mathrm{QP}}^{\mathrm{cube}}}{4\pi r_c^5} \tag{2}$$

where r_c is the distance between the center of Ag nanocube and the center of the QE, and V_{cube} is the volume of the

https://dx.doi.org/10.1021/acsphotonics.9b01499
ACS Photonics 2020, 7, 562−568

nanocube, and function ζ_{QP}^{cube} is called the polarizability factors and depends on the shape of the Ag nanocube.

Following the method of ref 47, the dipole moment in the QEs, P_{qd}, due to two-photon absorption has been calculated in reference[53,54] and is written as

$$P_{qd} = k_{12}\rho_{12}(1 + \Pi_{QP}^{cube})E_p e^{-i2\omega_1 t} = k_{12}\rho_{12}L(2\omega_1)E_p e^{-i2\omega_1 t} \quad (3)$$

where k_{12} is the two-photon coupling constant due to the transition and ρ_{12} is the two-photon density matrix element. $L(2\omega_1)$ is defined as the enhanced electric field caused by Ag nanocavity. Neglecting the dipole-SPP field in the Ag nanocube and SPP field produced by the Ag film, we get the SHG electric field produced by the QE as

$$E_{SHG}^{QE} = \frac{k_{12}\rho_{12}L(2\omega_1)E_p e^{-i2\omega_1 t}}{(4\pi r_{qd}^3/3)\varepsilon_b} \quad (4)$$

We calculated ρ_{12} due to two-photon emission by using the density matrix method.[47,55] We found the following expression for ρ_{12} as

$$\rho_{21} = \frac{i\Omega_{21}L(2\omega_1)}{(\gamma_2/2 - i\delta_{21} - i\Delta_s)} \quad (5)$$

The parameter $\delta_{12} = 2\omega_1 - \omega_{12}$ is called the probe detuning factor. The parameter Ω_{21} is called the Rabi frequencies. The parameter γ_2 is the spontaneous decay rate for state |2>. The parameter Δ_s is the Stark frequency and defined in ref 47. The intensity of the SHG electric field generated by the QE in the cavity is calculated as

$$I_{SHG}^{cavity} = (1/2)\varepsilon_0 c\sqrt{\varepsilon_b}\,|E_{SHG}^{QE}|^2 = \frac{(1/2)\varepsilon_0 c I_p\sqrt{\varepsilon_b}}{(4\pi r_{qd}^3/3)^2\varepsilon_b^2}\left|\left(\frac{ik_{12}\Omega_{21}L^2(2\omega_1)}{(\gamma_2/2 - i\delta_{21} - i\Delta_{s1})}\right)^2\right| \quad (6)$$

where I_p is the intensity of probe field. Similarly, we can calculate the SHG intensity when metallic nanocubes are absent. In other words, the hybrid structure is made of a metallic film with a spacer layer and monolayer WS_2 is placed on the spacer layer. In this case SHG intensity is denoted by I_{SHG}^{film}. The SHG intensity for this hybrid structure can be calculated from eq 6 by putting $\Pi_{QP}^{cube} = 0$. Let us calculate the SHG enhancement ratio due to presence of metallic nanocubes. It is defined as the ratio of I_{SHG}^{cavity} and I_{SHG}^{film} as $I_{ratio}^{SHG} = I_{SHG}^{cavity}/I_{SHG}^{film}$. Finally, the expression for the SHG ratio can be obtained as $I_{ratio}^{SHG} = L^4(2\omega_1)$, indicating that the SHG EF is proportional to the square of the local-field intensity in Ag nanocavity at SHG wavelength.

We have performed numerical simulations on the intensity of the SHG field produced by the nanohybrid. In simulations we have taken the dielectric constant of WS_2 as $\epsilon_q = 6.2$. The length of each side of the Ag-nanocube is about 75 nm. The plasmon frequency and the relaxation time for Ag are $\omega_p = 8.9$ eV and $\tau = 1.60 \times 10^{-14}$ s.[56] The value of the dielectric constant is $\epsilon_\infty = 5$.[56] Using these physical parameters we have calculated SPP resonance wavelengths of Ag nanocube (shown in Figure S7) and found as $\lambda_{DP}^{cube} = 620$ nm and $\lambda_{QP}^{cube} = 410$ nm, respectively. These values agree well with experimental values. The SPP resonance wavelength due to the metallic film is also calculated and found as $\lambda_{sp}^{film} = 120$ nm (see the Supporting Information for more calculated details).

In Figure 5a, the calculated enhancement ratio (I_{ratio}^{SHG}) as a function of λ_{exc} is plotted by a red curve. It shows that a good agreement between the theory and the experimental data. Note that the data in theoretical and experimental is a qualitative basis but not a quantitative basis. In general, under harmonic resonance in pure metal NPs, enhanced SHG is attributed to the improved emission efficiency, called antenna effect. The SHG intensity is in proportional to the local-field intensity, written as $I_{ratio}^{SHG} \propto L^2(2\omega_1)$.[28] Similar to the antenna effect, the SHG emission efficiency from a monolayer WS_2 is improved by the enhanced local-field $L(2\omega_1)$, as shown in eq 4 in the monolayer WS_2–Ag nanocavity nanohybrids. More importantly, unlike pure metal arrays, the source of SHG (P_{SHG}) in nanohybrids is also enhanced, which is shown in the enhanced density matrix element in eq 5. It is also proportional to the local-field intensity. Therefore, under two cooperative effects, harmonic resonance enhanced SHG intensity in nanohybrid is in proportion to the square of the local-field intensity. In experiment, a 2-order of magnitude enhancement can be achieved. In comparison with the harmonic resonance enhanced SHG in pure metal NPs, a novel SHG enhancement mechanism is presented. It is known that SHG signals actually contain not only dipolar terms but also multipolar ones, such as quadrupolar response. However, the relative magnitude of contributions from the quadrupole with respect to the dipole is generally quite weak. Therefore, our finding also can be used for enhancing the quadrupole signal by dipole–quadrupole interaction in hybrid nanostructure, which has potential implications for directional nonlinear generation.[57]

In conclusion, the harmonic resonance enhanced SHG from a monolayer WS_2 coupled to a plasmonic nanocavity is studied experimentally and theoretically. The nanocavity consists of single Ag nanocubes and an Al_2O_3–Ag film. A monolayer WS_2 is placed between the Ag nanocubes and the Al_2O_3 film. When the resonance wavelength of nanocavity is overlapped well with the SHG wavelength at 410 nm from the monolayer WS_2, a ~300-fold SHG enhancement is achieved. For understanding the SHG enhancement mechanism, the quantum mechanical density matrix method has been used to develop a theory for the SHG. It is found that SHG intensity is proportional to the square of the local-field intensity of Ag NPoM nanocavity under the dipole–quadrupole interaction. Specifically, the source of SHG in the monolayer WS_2 is enhanced in proportional to the local-field intensity of Ag nanocavity. While the SHG emission efficiency can also be enhanced by the local-field intensity, known as antenna effect. It presents a novel SHG enhancement mechanism, which has potential applications in nonlinear devices and hybrid nonlinear structures.

■ ASSOCIATED CONTENT

Supporting Information

The Supporting Information is available free of charge at https://pubs.acs.org/doi/10.1021/acsphotonics.9b01499.

The Raman spectrum of the WS_2 flake; The size distribution of the Ag nanocubes; Simulations of scattering, Scattering spectra of nanocavity before and after SHG measurement; Correlation between SHG EF and the scattering peak; Polarization property and SH collection efficiency of single nanocavities; The details of theoretical modeling; Estimation of the SHG conversion efficiency (PDF)

https://dx.doi.org/10.1021/acsphotonics.9b01499
ACS Photonics 2020, 7, 562–568

AUTHOR INFORMATION

Corresponding Authors

Kai Wang − *Wuhan National Laboratory for Optoelectronics and School of Physics, Huazhong University of Science and Technology, Wuhan 430074, China;* orcid.org/0000-0003-2122-1294; Email: kale_wong@hust.edu.cn

Mahi R. Singh − *Department of Physics and Astronomy, The University of Western Ontario, London N6G 3K7, Canada;* orcid.org/0000-0003-0930-4003; Email: msingh@uwo.ca

Peixiang Lu − *Hubei Key Laboratory of Optical Information and Pattern Recognition, Wuhan Institute of Technology, Wuhan 430205, China; Wuhan National Laboratory for Optoelectronics and School of Physics, Huazhong University of Science and Technology, Wuhan 430074, China; CAS Center for Excellence in Ultra-intense Laser Science, Shanghai 201800, China*; Email: lupeixiang@hust.edu.cn

Authors

Xiaobo Han − *Hubei Key Laboratory of Optical Information and Pattern Recognition, Wuhan Institute of Technology, Wuhan 430205, China*

Patrick D. Persaud − *Department of Physics and Astronomy, The University of Western Ontario, London N6G 3K7, Canada*

Xiangyuan Xing − *Wuhan National Laboratory for Optoelectronics and School of Physics, Huazhong University of Science and Technology, Wuhan 430074, China*

Weiwei Liu − *Wuhan National Laboratory for Optoelectronics and School of Physics, Huazhong University of Science and Technology, Wuhan 430074, China;* orcid.org/0000-0001-9451-1968

Hua Long − *Wuhan National Laboratory for Optoelectronics and School of Physics, Huazhong University of Science and Technology, Wuhan 430074, China*

Fang Li − *Hubei Key Laboratory of Optical Information and Pattern Recognition, Wuhan Institute of Technology, Wuhan 430205, China*

Bing Wang − *Wuhan National Laboratory for Optoelectronics and School of Physics, Huazhong University of Science and Technology, Wuhan 430074, China*

Complete contact information is available at: https://pubs.acs.org/10.1021/acsphotonics.9b01499

Notes

The authors declare no competing financial interest.

ACKNOWLEDGMENTS

This work was supported by National Natural Science Foundation of China (Nos. 11774115, 11904271, and 91850113) and the 973 Programs under Grant 2014CB921301 and the Campus Science Foundation Research Project of Wuhan Institute of Technology (No. K201822). One of the authors (M.R.S.) is thankful to the Natural Sciences and Engineering Research Council of Canada (NSERC) for the research grant. We thank Prof. Jun Zhou and Dr. Xiang Gao for Al_2O_3 film fabrication. Special thanks to the Analytical and Testing Center of HUST, the Center of Micro-Fabrication and Characterization (CMFC), and the Center for Nanoscale Characterization and Devices (CNCD) of WNLO for using their facilities.

REFERENCES

(1) Boyd, R. W. *Nonlinear Optics*, 2nd ed.; Academic Press, 2003.

(2) Hu, H.; Wang, K.; Long, H.; Liu, W.; Wang, B.; Lu, P. Precise determination of the crystallographic orientations in single ZnS nanowires by second-harmonic generation microscopy. *Nano Lett.* **2015**, *15*, 3351−3357.

(3) Yin, X.; Ye, Z.; Chenet, D. A.; Ye, Y.; O'Brien, K.; Hone, J. C.; Zhang, X. Edge nonlinear optics on a MoS_2 atomic monolayer. *Science* **2014**, *344*, 488−490.

(4) Dutto, F.; Raillon, C.; Schenk, K.; Radenovic, A. Nonlinear optical response in single alkaline niobate nanowires. *Nano Lett.* **2011**, *11*, 2517−2521.

(5) Buckley, S.; Radulaski, M.; Petykiewicz, J.; Lagoudakis, K. G.; Kang, J.-H.; Brongersma, M.; Biermann, K.; Vučković, J. Second-harmonic generation in GaAs photonic crystal cavities in (111) b and (001) crystal orientations. *ACS Photonics* **2014**, *1*, 516−523.

(6) Zielinski, M.; Oron, D.; Chauvat, D.; Zyss, J. Second-harmonic generation from a single core/shell quantum dot. *Small* **2009**, *5*, 2835−2840.

(7) Hsieh, C.-L.; Pu, Y.; Grange, R.; Laporte, G.; Psaltis, D. Imaging through turbid layers by scanning the phase conjugated second harmonic radiation from a nanoparticle. *Opt. Express* **2010**, *18*, 20723−20731.

(8) Campagnola, P. J.; Loew, L. M. Second-harmonic imaging microscopy for visualizing biomolecular arrays in cells, tissues and organisms. *Nat. Biotechnol.* **2003**, *21*, 1356−1360.

(9) Pantazis, P.; Maloney, J.; Wu, D.; Fraser, S. E. Second harmonic generating (SHG) nanoprobes for in vivo imaging. *Proc. Natl. Acad. Sci. U. S. A.* **2010**, *107*, 14535−14540.

(10) Han, X.; Wang, K.; Long, H.; Hu, H.; Chen, J.; Wang, B.; Lu, P. Highly sensitive detection of the lattice distortion in single bent ZnO nanowires by second-harmonic generation microscopy. *ACS Photonics* **2016**, *3*, 1308−1314.

(11) Li, Y.; Rao, Y.; Mak, K. F.; You, Y.; Wang, S.; Dean, C. R.; Heinz, T. F. Probing symmetry properties of few-layer MoS_2 and h-BN by optical second-harmonic generation. *Nano Lett.* **2013**, *13*, 3329−3333.

(12) Ren, M. L.; Agarwal, R.; Nukala, P.; Liu, W.; Agarwal, R. Nanotwin detection and domain polarity determination via optical second harmonic generation polarimetry. *Nano Lett.* **2016**, *16*, 4404−4409.

(13) Neeman, L.; Ben-Zvi, R.; Rechav, K.; Popovitz-Biro, R.; Oron, D.; Joselevich, E. Crystallographic mapping of guided nanowires by second harmonic generation polarimetry. *Nano Lett.* **2017**, *17*, 842−850.

(14) Richter, J.; Steinbruck, A.; Zilk, M.; Sergeyev, A.; Pertsch, T.; Tunnermann, A.; Grange, R. Core-shell potassium niobate nanowires for enhanced nonlinear optical effects. *Nanoscale* **2014**, *6*, 5200−5207.

(15) Huang, H.; Ke, S. L.; Wang, B.; Long, H.; Wang, K.; Lu, P. X. Numerical study on plasmonic absorption enhancement by a rippled graphene sheet. *J. Lightwave Technol.* **2017**, *35*, 320−324.

(16) Marin, B. C.; Hsu, S.-W.; Chen, L.; Lo, A.; Zwissler, D. W.; Liu, Z.; Tao, A. R. Plasmon-enhanced two-photon absorption in photoluminescent semiconductor nanocrystals. *ACS Photonics* **2016**, *3*, 526−531.

(17) Long, H.; Bao, L.; Habeeb, A. A.; Lu, P. Effects of doping concentration on the surface plasmonic resonances and optical nonlinearities in AGZO nano-triangle arrays. *Opt. Quantum Electron.* **2017**, *49*, 345.

(18) Hyun, J. K.; Kang, T.; Baek, H.; Oh, H.; Kim, D.-S.; Yi, G.-c. Enhanced second harmonic generation by coupling to exciton ensembles in Ag-coated ZnO nanorods. *ACS Photonics* **2015**, *2*, 1314−1319.

(19) Liu, X.; Zhang, Q.; Chong, W. K.; Yip, J. N.; Wen, X.; Li, Z.; Wei, F.; Yu, G.; Xiong, Q.; Sum, T. C. Cooperative enhancement of second-harmonic generation from a single CdS nanobelt-hybrid plasmonic structure. *ACS Nano* **2015**, *9*, 5018−26.

(20) Grinblat, G.; Rahmani, M.; Cortes, E.; Caldarola, M.; Comedi, D.; Maier, S. A.; Bragas, A. V. High-efficiency second harmonic generation from a single hybrid ZnO nanowire/Au plasmonic nano-oligomer. *Nano Lett.* **2014**, *14*, 6660−6665.

(21) Ren, M. L.; Liu, W.; Aspetti, C. O.; Sun, L.; Agarwal, R. Enhanced second-harmonic generation from metal-integrated semiconductor nanowires via highly confined whispering gallery modes. *Nat. Commun.* **2014**, *5*, 5432.
(22) Hu, H.; Wang, K.; Long, H.; Han, X.; Chen, J.; Wang, B.; Lu, P. Concentrated second-harmonic generation from a single Al-covered ZnS nanobelt. *Laser Photonics Rev.* **2017**, *11*, 1600263.
(23) Yang, Z.; Cao, W.; Chen, X.; Zhang, J.; Mo, Y.; Xu, H.; Mi, K.; Zhang, Q.; Lan, P.; Lu, P. All-optical frequency-resolved optical gating for isolated attosecond pulse reconstruction. *Opt. Lett.* **2020**, *45*, 567.
(24) Aouani, H.; Rahmani, M.; Navarro-Cia, M.; Maier, S. A. Third-harmonic-upconversion enhancement from a single semiconductor nanoparticle coupled to a plasmonic antenna. *Nat. Nanotechnol.* **2014**, *9*, 290−4.
(25) Liu, W.; Li, X.; Song, Y.; Zhang, C.; Han, X.; Long, H.; Wang, B.; Wang, K.; Lu, P. Cooperative enhancement of two-photon-absorption-induced photoluminescence from a 2D perovskite-microsphere hybrid dielectric structure. *Adv. Funct. Mater.* **2018**, *28*, 1707550.
(26) Li, X.; Liu, W.; Song, Y.; Long, H.; Wang, K.; Wang, B.; Lu, P. Two-photon-pumped high-quality, single-mode vertical cavity lasing based on perovskite monocrystalline films. *Nano Energy* **2020**, *68*, 104334.
(27) Chen, J.; Wang, K.; Long, H.; Hu, H.; Han, X.; Wang, B.; Lu, P. Quantitatively extracting the contribution of asymmetric local-field to $\chi^{(2)}$ in cross-shaped Ag nanoholes. *Opt. Express* **2017**, *25*, 1296−1307.
(28) Metzger, B.; Gui, L. L.; Fuchs, J.; Floess, D.; Hentschel, M.; Giessen, H. Strong enhancement of second harmonic emission by plasmonic resonances at the second harmonic wavelength. *Nano Lett.* **2015**, *15*, 3917−3922.
(29) Ma, C.; Yan, J.; Wei, Y.; Liu, P.; Yang, G. Enhanced second harmonic generation in individual barium titanate nanoparticles driven by mie resonances. *J. Mater. Chem. C* **2017**, *5*, 4810−4819.
(30) Yang, K.-Y.; Butet, J.; Yan, C.; Bernasconi, G. D.; Martin, O. J. F. Enhancement mechanisms of the second harmonic generation from double resonant aluminum nanostructures. *ACS Photonics* **2017**, *4*, 1522−1530.
(31) Thyagarajan, K.; Rivier, S.; Lovera, A.; Martin, O. J. F. Enhanced second-harmonic generation from double resonant plasmonic antennae. *Opt. Express* **2012**, *20*, 12860−12865.
(32) Harutyunyan, H.; Volpe, G.; Quidant, R.; Novotny, L. Enhancing the nonlinear optical response using multifrequency gold-nanowire antennas. *Phys. Rev. Lett.* **2012**, *108*, 217403.
(33) Cong, C.; Shang, J.; Wang, Y.; Yu, T. Optical properties of 2D semiconductor WS_2. *Adv. Opt. Mater.* **2018**, *6*, 1700767.
(34) Allain, A.; Kang, J.; Banerjee, K.; Kis, A. Electrical contacts to two-dimensional semiconductors. *Nat. Mater.* **2015**, *14*, 1195−205.
(35) Ciracì, C.; Hill, R. T.; Mock, J. J.; Urzhumov, Y.; Fernández-Domínguez, A. I.; Maier, S. A.; Pendry, J. B.; Chilkoti, A.; Smith, D. R. Probing the ultimate limits of plasmonic enhancement. *Science* **2012**, *337*, 1072−1074.
(36) Hoang, T. B.; Akselrod, G. M.; Argyropoulos, C.; Huang, J.; Smith, D. R.; Mikkelsen, M. H. Ultrafast spontaneous emission source using plasmonic nanoantennas. *Nat. Commun.* **2015**, *6*, 1−7.
(37) Sigle, D. O.; Mertens, J.; Herrmann, L. O.; Bowman, R. W.; Ithurria, S.; Dubertret, B.; Shi, Y.; Yang, H. Y.; Tserkezis, C.; Aizpurua, J.; Baumberg, J. J. Monitoring morphological changes in 2D monolayer semiconductors using atom-thick plasmonic nanocavities. *ACS Nano* **2015**, *9*, 825−830.
(38) Yashima, S.; Sugimoto, H.; Takashina, H.; Fujii, M. Fluorescence enhancement and spectral shaping of silicon quantum dot monolayer by plasmonic gap resonances. *J. Phys. Chem. C* **2016**, *120*, 28795−28801.
(39) Akselrod, G. M.; Weidman, M. C.; Li, Y.; Argyropoulos, C.; Tisdale, W. A.; Mikkelsen, M. H. Efficient nanosecond photoluminescence from infrared PbS quantum dots coupled to plasmonic nanoantennas. *ACS Photonics* **2016**, *3*, 1741−1746.
(40) Akselrod, G. M.; Huang, J.; Hoang, T. B.; Bowen, P. T.; Su, L.; Smith, D. R.; Mikkelsen, M. H. Large-area metasurface perfect absorbers from visible to near-infrared. *Adv. Mater.* **2015**, *27*, 8028−8034.
(41) Kleemann, M. E.; Chikkaraddy, R.; Alexeev, E. M.; Kos, D.; Carnegie, C.; Deacon, W.; de Pury, A. C.; Grosse, C.; de Nijs, B.; Mertens, J.; Tartakovskii, A. I.; Baumberg, J. J. Strong-coupling of WSe_2 in ultra-compact plasmonic nanocavities at room temperature. *Nat. Commun.* **2017**, *8*, 1296.
(42) Zheng, D.; Zhang, S.; Deng, Q.; Kang, M.; Nordlander, P.; Xu, H. Manipulating coherent plasmon-exciton interaction in a single silver nanorod on monolayer WSe_2. *Nano Lett.* **2017**, *17*, 3809−3814.
(43) Akselrod, G. M.; Ming, T.; Argyropoulos, C.; Hoang, T. B.; Lin, Y.; Ling, X.; Smith, D. R.; Kong, J.; Mikkelsen, M. H. Leveraging nanocavity harmonics for control of optical processes in 2D semiconductors. *Nano Lett.* **2015**, *15*, 3578−3584.
(44) Li, B.; He, Y.; Lei, S.; Najmaei, S.; Gong, Y.; Wang, X.; Zhang, J.; Ma, L.; Yang, Y.; Hong, S.; Hao, J.; Shi, G.; George, A.; Keyshar, K.; Zhang, X.; Dong, P.; Ge, L.; Vajtai, R.; Lou, J.; Jung, Y. J.; Ajayan, P. M. Scalable transfer of suspended two-dimensional single crystals. *Nano Lett.* **2015**, *15*, 5089−5097.
(45) Huang, S.; Ming, T.; Lin, Y.; Ling, X.; Ruan, Q.; Palacios, T.; Wang, J.; Dresselhaus, M.; Kong, J. Ultrasmall mode volumes in plasmonic cavities of nanoparticle-on-mirror structures. *Small* **2016**, *12*, 5190−5199.
(46) Wen, X.; Xu, W.; Zhao, W.; Khurgin, J. B.; Xiong, Q. Plasmonic hot carriers-controlled second harmonic generation in WSe_2 bilayers. *Nano Lett.* **2018**, *18*, 1686−1692.
(47) Singh, M. R. Enhancement of the second-harmonic generation in a quantum dot-metallic nanoparticle hybrid system. *Nanotechnology* **2013**, *24*, 125701.
(48) Sarid, D.; Challener, W. *Modern Introduction to Surface Plasmons*; Cambridge University Press, 2010.
(49) Singh, M. R.; Cox, J. D.; Brzozowski, M. Photoluminescence and spontaneous emission enhancement in metamaterial nanostructures. *J. Phys. D: Appl. Phys.* **2014**, *47*, No. 085101.
(50) Singh, M. R.; Guo, J.; J. Cid, J. M.; De Hoyos Martinez, J. E. Control of fluorescence in quantum emitter and metallic nanoshell hybrids for medical applications. *J. Appl. Phys.* **2017**, *121*, No. 094303.
(51) Singh, M. R.; Sekhar, M. C.; Balakrishnan, S.; Masood, S. Medical applications of hybrids made from quantum emitter and metallic nanoshell. *J. Appl. Phys.* **2017**, *122*, No. 034306.
(52) Guo, J.; Black, K.; Hu, J.; Singh, M. Study of plasmonics in hybrids made from a quantum emitter and double metallic nanoshell dimer. *J. Phys.: Condens. Matter* **2018**, *30*, 185301.
(53) Meystre, P.; Sargent, M. *Elements of Quantum Optics*; Springer: Berlin, 2007.
(54) de Garcia, A. G.; Meystre, P.; Salomaa, R. R. E. Time-delayed probe spectroscopy in two-photon−pumped systems. *Phys. Rev. A: At., Mol., Opt. Phys.* **1985**, *32*, 1531−1540.
(55) Meystre, P. S. M. *Elements of Quantum Optics*; Springer Science & Business Media, 2007.
(56) Yang, H. U.; D'Archangel, J.; Sundheimer, M. L.; Tucker, E.; Boreman, G. D.; Raschke, M. B. Optical dielectric function of silver. *Phys. Rev. B: Condens. Matter Mater. Phys.* **2015**, *91*, 235137.
(57) Rose, A.; Huang, D.; Smith, D. R. Nonlinear interference and unidirectional wave mixing in metamaterials. *Phys. Rev. Lett.* **2013**, *110*, No. 063901.

https://dx.doi.org/10.1021/acsphotonics.9b01499
ACS Photonics 2020, 7, 562−568